



Carbon Nanotube Degradation in Macrophages: Live Nanoscale Monitoring and Understanding of Biological Pathway

Dan Elgrabli, Walid Dachraoui, Cécilia Ménard-Moyon, Xiao Jie Liu, Dominique Begin, Sylvie Bégin-Colin, Alberto Bianco, Florence Gazeau, Damien Alloyeau

► To cite this version:

Dan Elgrabli, Walid Dachraoui, Cécilia Ménard-Moyon, Xiao Jie Liu, Dominique Begin, et al.. Carbon Nanotube Degradation in Macrophages: Live Nanoscale Monitoring and Understanding of Biological Pathway. ACS Nano, 2015, 9 (10), pp.10113-10124. 10.1021/acsnano.5b03708 . hal-02557774

HAL Id: hal-02557774

<https://hal.science/hal-02557774>

Submitted on 9 Nov 2023

HAL is a multi-disciplinary open access archive for the deposit and dissemination of scientific research documents, whether they are published or not. The documents may come from teaching and research institutions in France or abroad, or from public or private research centers.

L'archive ouverte pluridisciplinaire **HAL**, est destinée au dépôt et à la diffusion de documents scientifiques de niveau recherche, publiés ou non, émanant des établissements d'enseignement et de recherche français ou étrangers, des laboratoires publics ou privés.

This document is confidential and is proprietary to the American Chemical Society and its authors. Do not copy or disclose without written permission. If you have received this item in error, notify the sender and delete all copies.

Carbon nanotube degradation in macrophages: live nanoscale monitoring and understanding of biological pathway

Journal:	ACS Nano
Manuscript ID:	nn-2015-03708r.R1
Manuscript Type:	Article
Date Submitted by the Author:	n/a
Complete List of Authors:	Elgrabli, Daan; Université paris 7, MSC dachraoui, walid; Université Paris 7 Denis Diderot, MPQ Ménard-Moyon, Cécilia; CNRS, UPR9021, ICT Liu, Xiao Jie; Université de Strasbourg, Begin, Dominique; CNRS, Begin-Colin, Sylvie; Université de Strasbourg, Bianco, Alberto; CNRS, UPR3572, Immunophatologie et Chimie Thérapeutiques Gazeau, Florence; Univeriste Paris-Diderot, Batiment Condorcet Alloyeau, Damien; Université Paris 7 Denis Diderot, Laboratoire Matériaux et Phénomènes Quantiques

SCHOLARONE™
Manuscripts

Carbon Nanotube Degradation in Macrophages: Live Nanoscale Monitoring and Understanding of Biological Pathway

*Dan Elgrabli^{1‡}, Walid Dachraoui^{2‡}, Cécilia Ménard-Moyon³, Xiao Jie Liu⁴, Dominique Bégin⁴,
Sylvie Bégin⁵, Alberto Bianco³, Florence Gazeau^{1*} and Damien Alloyeau^{2*}*

(1) Laboratoire Matière et Systèmes Complexes, UMR7057 CNRS/Université Paris Diderot,
Paris France.

(2) Laboratoire Matériaux et Phénomènes Quantiques, UMR7057 CNRS/Université Paris
Diderot, Paris France.

(3) CNRS, Institut de Biologie Moléculaire et Cellulaire, Laboratoire d’Immunopathologie et
Chimie Thérapeutique, 67000 Strasbourg, France

(4) Institut de Chimie et des Procédés pour L’Energie, l’Environnement et la Santé (ICPEES)
UMR 7515, Université de Strasbourg, 25 rue Becquerel, 67087 Strasbourg cedex 2 France

(5) Institut de Physique et de Chimie de Strasbourg (IPCMS) UMR 7504 CNRS-Université de
Strasbourg, 23 rue du Loess, BP 34 67034 Strasbourg cedex 2, France

KEYWORDS

Biodegradation, Carbon nanotubes, macrophages, genetic response, liquid-cell transmission electron microscopy, reactive oxygen species.

ABSTRACT

Despite numerous applications, the cellular-clearance mechanism of multi-walled carbon nanotubes (MWCNTs) has not been clearly established yet. Previous *in vitro* studies showed the ability of oxidative enzymes to induce nanotube degradation. Interestingly, these enzymes have the common capacity to produce reactive oxygen species (ROS). Here, we combined material and life science approaches for revealing an intra-cellular way taken by macrophages to degrade carbon nanotubes. We report the *in situ* monitoring of ROS-mediated-MWCNT degradation by liquid-cell transmission electron microscopy. Two degradation mechanisms induced by hydroxyl radicals were extracted from these unseen dynamic nanoscale investigations: a non-site-specific thinning process of the walls and a site-specific transversal drilling process on pre-existing defects of nanotubes. Remarkably, similar ROS-induced structural injuries were observed on MWCNTs after aging into macrophages from one to seven days. Beside unraveling oxidative transformations of MWCNT structure, we elucidated an important, albeit not exclusive, biological pathway for MWCNT degradation in macrophages, involving NOX₂ complex activation, superoxide production and hydroxyl radical attack, which highlights the critical role of oxidative stress in cellular processing of MWCNTs.

Although carbon nanotubes (CNTs) are one of the most promising nanomaterials for technological and pharmaceutical applications,^{1, 2} many grey areas remain on their life cycle in biological environments, notably regarding their biodegradation mechanisms that drastically impact their efficiency and innocuousness. In the last years, a few studies have investigated CNT biokinetics (translocation, biodistribution and clearance) *in vivo*,³⁻⁵ revealing that, like most nanomaterials, their “journey” in the organism mainly ends in macrophage cells in lung after intratracheal instillation,^{3, 6} or in liver and spleen after intravenous injection.^{7, 8} A slow degradation of CNTs seems to occur in phagosomes,^{3, 9} but the biochemical and structural processes involved in the degradation of graphitic nanostructures remain unclear. *In vitro* enzymatic biodegradation of CNTs have shown that horseradish peroxidase (HRP), an enzyme from plant, can oxidize single-walled CNTs (SWCNTs) in the presence of low levels of hydrogen peroxide.¹⁰ CNT biodegradation studies were then extended to other peroxidases such as myeloperoxidase (MPO)¹¹ present in neutrophils, eosinophil peroxidase (EPO)¹² and lactoperoxidase (LPO)¹³ expressed by goblet cells found in the epithelial lining of the respiratory tract as well as in many human exocrine secretions. The degradation mechanisms rely on the ability of MPO, EPO and LPO to convert hydrogen peroxide (H₂O₂) into hypochlorous, hypobromous and hypothiocyanous acids, respectively. As observed for microorganisms, SWCNTs can be entrapped by a network of chromatin and proteins outside the cells and undergo acellular MPO-mediated biodegradation.¹⁴ In the same way, non-enzymatic degradation medium constituted by phagolysosomal elements associated with H₂O₂ is also able to degrade CNTs.¹⁵ All these results emphasize the capacity of oxidant species to induce CNT degradation.. Kagan and coworkers have recently demonstrated the ability of lung macrophages to degrade CNTs in extra-cellular fluid using superoxide/Peroxynitrite

oxidative pathways.¹⁶ Here, we combined materials sciences and biological approaches to reveal another way taken by macrophages to degrade functionalized multi-walled carbon nanotubes (MWCNTs) in intra-cellular compartments, which also involves the oxidizing power of reactive oxygen species (ROS) produced by an enzymatic complex. On the one hand, *in situ* transmission electron microscopy (TEM) in liquid provided an unprecedented live monitoring of the ROS-induced damages in MWCNT structure. On the other hand molecular and chemical biology highlighted the crucial role of NADPH oxidase 2 (NOX₂) enzymatic complexes in the ROS-production mechanisms responsible for MWCNT degradation.

Results and discussion

Structural degradation of MWCNTs induced by ROS in macrophages.

We carried out TEM analyses of the structural degradation of MWCNTs as a function of their aging time (t_{ag}) in THP-1 cells differentiated into macrophages. These studies were performed with two types of nanomaterials: MWCNTs and MWCNTs filled with magnetic iron oxide nanoparticles (namely Fe@MWCNTs). These latter were synthesized with a high-yield two-step process.¹⁷ In both cases, MWCNTs were functionalized by arylation to introduce amino groups on the nanotube sidewall and to ensure a good dispersion in physiological media. In view of cytotoxicity assessments after 24h exposure to CNTs (Figure S1), we choose a dose of MWCNTs and Fe@MWCNTs of 5 $\mu\text{g}/\text{ml}$ inducing a cell-death degree below 5%. After t_{ag} of 3h, 24h, 48h and 168h, CNTs were extracted from cells to perform TEM observations. As can be seen in Figure 1a for MWCNTs and Figure S2 for Fe@MWCNTs, the graphitic nanostructures are deeply scarred by cells. The main stigmata of degradation processes are the presence of holes in the carbon walls. High resolution TEM allows confirming that these holes can be either drilled through one side or

through the whole nanotube structure (Figure S3a-c). The t_{ag} -dependent analyses of the percentage of perforated area (P_a , Figure 1b), the average surface area of holes (\bar{S} , Figure 1c) and the number of holes per surface unit (D , Figure 1d) provide a better overview of the degradation mechanisms. The degradation of MWCNTs quickly increases over time in cells, with P_a reaching 51 % after 168 h aging. However, the 25-fold increase of P_a when increasing t_{ag} from 3h to 168h is concomitantly due to the raise of \bar{S} and D , that vary as $t^{1/3}$ and $t^{1/2}$, respectively. As $P_a = \bar{S} \times D$, our measurements allows evaluating the respective weight of the nucleation and growth of holes on the expansion of structural damage in MWCNTs. The fast increase of D , yet slowed down by the coalescence of holes, reveals that MWCNTs present many energetically-affordable onset of degradation and indicates that the degradation mechanisms are not dominated by the expansion of holes drilled on sparse preferential sites. We also noted that the mean thickness of the nanotube walls was reduced by 15% after 168h in macrophages. Figure 1e shows that the amount of ROS quantified by 2',7'-dichlorodihydrofluorescein diacetate (DCFDA) is approximatively 3-fold increased when MWCNTs or Fe@MWCNTs are incubated 24h with THP-1-derived macrophages. This enhanced production of ROS is in agreement with previous studies on other macrophages¹⁸ and it highlights the possible role of these highly oxidative species in the degradation of exogenous nanomaterials.^{11, 19, 20} In order to test this hypothesis, we assessed the effects of N-acetyl-L-cysteine (NAC), a ROS scavenger inducer, on degradation of MWCNTs. NAC significantly reduced the cellular production of ROS, which was still 20% higher than the untreated control (Figure 1e). Interestingly, the presence of NAC substantially prevented the degradation of both MWCNTs and Fe@MWCNTs. Up to 3-fold decrease of P_a was measured after 48h intracellular aging in the presence of NAC, while both \bar{S} and D were also reduced (Figure 1b-d). This confirms that antioxidant inducers diminish both nucleation and growth of cell-induced damages in

1
2
3 MWCNTs. The kinetics and mechanisms of degradation of Fe@MWCNTs are very similar to the
4 ones of MWCNTs, suggesting that iron embedded into nanotubes do not interplay with the
5 degradation mechanisms. The relevance of all these statistical measurements was validated by
6 Kolmogorov-Smirnov tests (Figure S4).
7
8
9
10

11
12
13 As these important alterations of the graphitic structures could also modify the cytotoxicity effects
14 of CNTs over time, we evaluated if the products of degradation extracted from cells 24h after
15 exposure are more or less toxic than the original forms. Using Alamar blue assay, we compared
16 the lethal dose inducing 50% cell death (LD50) for MWCNTs, Fe@MWCNTs and their
17 degradation products (namely dMWCNT and dFe@MWCNT respectively). Interestingly, Figure
18 S5 shows that the degradation products are less toxic (LD50 was 47.2 and 54.3 $\mu\text{g/ml}$ for
19 dMWCNT and dFe@MWCNT, respectively) than the original nanosystems (LD50 was 27.7
20 $\mu\text{g/ml}$ for both MWCNTs and Fe@MWCNT), revealing that cell processing of MWCNTs tends
21 to minimize their cytotoxicity.
22
23
24
25
26
27
28
29
30
31
32
33
34

35
36 Reducing the gap between *in vitro* and *in vivo* investigations is an essential prerequisite to fully
37 understand CNT lifecycle in the organism and to exploit this knowledge in biomedicine. As a first
38 step, we compared the degradations of graphitic structures in cell cultures and in animals. Rats
39 were exposed to MWCNTs *via* intra-tracheal instillation and *ex vivo* TEM analyses revealed the
40 presence of exogenous nanomaterials in macrophages of the lungs and the lymph nodes, 7 days
41 after the exposure (figure S6). However, by analysing closely these TEM experiments, we can
42 clearly observed the presence of many holes in the structure of the tubes. Therefore, these highly
43 perforated nanotubes indicate that the oxidative degradation processes analysed over time through
44 *in vitro* approach, are very similar to the structural alterations of CNTs occurring *in vivo*.
45
46
47
48
49
50
51
52
53
54
55
56
57
58
59
60

***In situ* nano-scale monitoring of the ROS-induced damages in MWCNTs.**

Liquid-cell TEM has provided the opportunity to follow nanoscale processes at the interfaces between liquids and solids, opening many avenues in both material and life sciences.^{21, 22} It is well-established that the electron-beam irradiation of water generates the following primary products by radiolysis: hydrated electrons (e_{h^-}), hydrogen radicals (H^\bullet), hydroxyl radicals (OH^\bullet), dihydrogen (H_2), H_2O_2 , hydronium ions (H_3O^+), hydroperoxyl radicals (HO_2^\bullet).²³ When nanoscale analyses are performed in water, these species are uniformly distributed within the irradiated region with concentrations varying as sub-linear power laws of the electron-dose rate (\dot{d}).²⁴ The straightforward control over the local production of strong reducing agent (e_{h^-} , H^\bullet) has been deeply exploited to study the nucleation and growth of metal nanoparticles *via* the reduction of metallic precursor.²⁵⁻²⁹ Here, we investigated the degradation mechanisms of MWCNTs and Fe@MWCNTs in water under electron beam irradiation and we identified the oxidizing species involved in this chemical attack. Structural modifications of MWCNTs was simultaneously generated and imaged in scanning transmission electron microscopy (STEM) mode at 80 kV. Signals were collected with a high annular angular dark field (HAADF) detector. The high signal-to-noise ratio of STEM-HAADF imaging, in which \dot{d} is proportional to the square of the magnification, allows distinguishing two mechanisms in the degradation of MWCNTs. Figure 2a illustrates that the cylindrical nanostructures sustain a wall-by-wall thinning until breaking of the tube. Interestingly, this erosion occurs all along the irradiated surfaces of CNTs. Intensity profiles measured perpendicularly to the anisotropy axis also reveals that both inner and outer sides of the MWCNTs are attacked, suggesting that chemical species are also generated inside the inner cavity when the electron beam pass through the nanotubes. This induces a reduction of the outer diameter

and an increase of the inner diameter that were measured to be linear with time (Figure 2b). By defining the speed of thinning process as the slope of the linear relation of diameters and time, we demonstrated that the kinetic of degradation is enhanced with \dot{d} . For example, the speed of degradation for the outer diameter was boosted from 0.6 nm/s to 2.3 nm/s, when stepping up \dot{d} from $3.4 \cdot 10^7 \text{ Gy.s}^{-1}$ (magnification of 150k) to $2.4 \cdot 10^8 \text{ Gy.s}^{-1}$ (magnification of 400k) (Figure 2c). Together with this non-site-specific thinning, MWCNTs sometimes endure more severe damages consisting in transversal drillings of the walls. Figure 3a shows that this second degradation mechanism can either generate spherical holes if the drilling axis is almost perpendicular to the tube axis or can tear the nanotubes lengthwise for more grazing drilling angles, pulling out together many walls from the tubes and creating elongated holes. As these drilling processes were not systematically observed, one can reasonably assume that pre-existing defects in the MWCNTs (pentagon-hexagon pairs, atomic vacancies, dislocations, presence of functional groups that lead to the formation of sp^3 hybridized carbon atoms, etc.), that are more reactive due to deformation, may favor this faster degradation mechanisms. This assumption is strengthened by the degradation mechanisms of Fe@MWCNTs that in rare cases present iron oxide nanoparticles inserted in between the nanotubes walls (Figure 3b). As observed by *ex situ* HRTEM (Figure S7), the MWCNT structure presents a high rate of crystalline defects in these interface areas. These highly-reactive zones systematically serve as onset for transversal drilling by tearing along the interface between the tube and the nanoparticles. Figure 3b (100 and 120 minutes of observation) also illustrates that the degradation of the last remaining walls of nanotubes frequently occurs through a slower wall-by-wall thinning. Although the encapsulated iron-oxide nanoparticles move inside the MWCNTs under beam irradiation, their dispersion in the liquid cell is possible only after the

1
2
3 rupture of the tubes, illustrating the potential of biodegradable MWCNTs for drug delivery
4 applications.³⁰
5
6

7
8
9 It is worth to note that no structural alteration was observed when MWCNTs and Fe@MWCNTs
10 were irradiated for several hours with the same optical conditions under vacuum (Figure 4a). As
11 the energy of incident electrons was below the knock-on-damage threshold in MWCNTs, the
12 degradation processes observed in water are unambiguously induced by chemical reactions.
13
14 Furthermore, both wall-by-wall thinning and drilling mechanisms were exclusively observed in
15 the irradiated areas showing the short life-time and very low diffusion of the involved chemical
16 species. Schneider *et al.* have calculated that among the radiolysis products only the highly reactive
17 species (e_h^- , H^\bullet , OH^\bullet) are strictly restricted to the irradiated region. Thus, the strong oxidation
18 potential of OH^\bullet makes it the most likely candidate for the chemical degradation of MWCNTs.
19
20 The dose-dependent concentration of this short-lived ROS, that varies as $\dot{d}^{0.46}$,²⁴ is also consistent
21 with the degradation boosting observed for higher magnifications. This damaging role of OH^\bullet was
22 definitely confirmed by the long-term stability of MWCNTs in ethanol (Figure 4b), in which
23 ionizing radiations generate peroxy radicals, but no OH^\bullet .³¹
24
25
26
27
28
29
30
31
32
33
34
35
36
37
38
39

40
41 Additionally, the two mechanisms of degradation extracted from these *in situ* TEM observations
42 are in agreement with previous spectroscopy studies that suggested two concomitant destructive
43 interactions of OH^\bullet with MWCNTs³²: 1) OH^\bullet could preferentially attack MWCNTs at the defect
44 sites to produce carboxylic acid groups leading to disordered and perforated walls. Note that, the
45 covalent functionalization by arylation induces the rehybridization of sp^2 carbon atoms to sp^3 , thus
46 increasing the amount of defects and the reactivity of the MWCNTs towards OH^\bullet in the vicinity
47 of the functionalized carbon atoms. 2) OH^\bullet could also insert a significant amount of hydroxyl
48 groups on unsaturated C=C bonds of the nanotube sidewalls by electrophilic addition reaction, that
49
50
51
52
53
54
55
56
57
58
59
60

are then converted into quinones and eventually carboxylic acids. MWCNT functionalization also imparts enhanced hydroxyl radical capture ability, in particular OH^\bullet .³³⁻³⁵ Interestingly, the presence of hydroxyl and carbonyl functions was detected on MWCNTs extracted from rat lung³. These oxygen-containing functional groups emphasize on the putative role of OH^\bullet in MWCNT degradation in cells. Although the dynamic processes observed *in situ* are much faster than those occurring in cells because of the higher concentration of ROS (around 10^{-5} M^{24} *versus* less than 10^{-6} M in phagosome³⁶), the two mechanisms of degradation can also explain the thinner and highly-perforated walls of the tubes extracted from macrophages. The non-site-specific thinning certainly allows the exposition of sub-surface defects to ROS resulting in the drilling of many holes in MWCNTs.

Biological pathway for MWCNT degradation by macrophages.

As both *in situ* and *in vitro* nanoscale studies suggest the crucial role of ROS in the degradation of MWCNTs, we focused on the biological pathway for the production of ROS and particularly OH^\bullet . In cells, MWCNTs are degraded into phagosomes,³ and NOX_2 complex is well known to be associated with the plasma and the phagosomal membranes. This enzymatic complex was described to be a biocatalyst of the reduction of molecular oxygen to generate superoxide $\text{O}_2^{\bullet-}$ that can dismute to generate ROS species.³⁷ NOX -family enzymes are likely to be involved in a variety of physiological events including cell proliferation, host defense, differentiation, apoptosis, senescence and activation of growth-related signaling pathways.³⁷ NOX_2 complex consists of a large association of glycoproteins named $\text{NOX}_{2\alpha}$ (or gp22phox), $\text{NOX}_{2\beta}$ (or gp91phox) and cytosolic proteins, namely p67phox, p47phox, p40phox and Rac.³⁷ To assess the involvement of NOX_2 complex into the degradation processes, macrophages were exposed for 24h to $5 \mu\text{g/ml}$ of MWCNTs or Fe@MWCNTs and total ribonucleic acid (RNA) were extracted. The mRNA of

NOX_{2α}, NOX_{2β}, p67phox, p47phox and p40phox were quantified by polymerase chain reaction (PCR) (Figure 5a). The mRNAs of all of these proteins were approximatively induced two times as compared to the untreated cells. The protein level for NOX_{2β} was also assessed by western blot analysis. Both inductions at the genetic and protein levels are in good agreement (Figure S8). Remarkably in the presence of NAC, no significant or much lower inductions were measured. Together with the nanoscale investigations of the degraded MWCNTs, the biological response of macrophages indicates a MWCNT-induced activation of NOX₂ complex and a subsequent production of ROS with the purpose of degrading exogenous nanostructures. The addition of NAC in the cellular medium inhibits the existing ROS and perturbs the retroactivity of ROS-production by NOX₂, resulting in the low activity of this complex and the lower capacity of cells to degrade MWCNTs.

When activated, NOX₂ complex is the most important source of ROS in phagocytes by O₂^{•−} production³⁶. In the presence of superoxide dismutase (SOD), O₂^{•−} can dismute into H₂O₂. As described by Haber-Weiss reaction, in the presence of iron, O₂^{•−} and H₂O₂ produce OH[•]. We evaluated this possible production pathway of OH[•] by quantifying SOD mRNA (Figure 5b). Cu-SOD that is preferentially located into cytoplasm was induced 1.7 times as compared to control. NAC did not change mRNA level of this protein. Mn-SOD that is preferentially located into phagosome, was induced more than 2 times for MWCNTs and Fe@MWCNTs, but the presence of NAC annihilates this enhanced-mRNA level. Note that mRNA of glutathione S-transferase (GSTP-1), a well-known antioxidant, also increases most probably to regulate ROS production (Figure 5b). Remarkably, Fe³⁺-catalyzed Haber-Weiss reaction³¹ and its metabolism seems to play a role in the regulation of CNTs degradation *via* the production of iron storage proteins, such as ferritin. Indeed both light chain (FerL) and heavy chain (FerH) of ferritin mRNA were induced by

MWCNT and Fe@MWCNT exposure (Figure 5c), as well as the protein level for FerH (figure S8). Nevertheless, FerH mRNA was much less increased with Fe@MWCNTs than with MWCNTs. This phenomenon indicates that the regulation of Fe^{3+} involved in the production of OH^{\bullet} , is influenced by the presence of magnetite nanoparticles (composed of both Fe^{2+} and Fe^{3+} ions) inside the nanotubes. With iron-free nanotubes, the cells need to provide more Fe^{3+} ions and then produce more ferritin. With Fe@MWCNT, the cells reduce the endogenous production of Fe^{3+} ions, because of the exogenous $\text{Fe}^{3+}/\text{Fe}^{2+}$ pool inside the tubes. These perturbations in the iron-production mechanisms employed by macrophages to degrade carbon nanotubes could generate different production rate of OH^{\bullet} and could then be responsible for the slightly different degradation kinetics of MWCNTs and Fe@MWCNTs. For example, after 168h of incubation only 40.5% of total surface area for Fe@MWCNTs versus 51.1% for MWCNTs was degraded (Figure 1b).

As iNOS and MPO proteins were described to take part in CNT biodegradation,^{10, 16} their roles were also investigated. Peroxynitrite-induced CNTs degradation was reported to play a significant, but not exclusive, role in the biodegradation process,¹⁶ Peroxynitrite production in cells is due to a non-enzymatic reaction of superoxide radicals and NO^{\bullet} .^{38, 39} In presence of MWCNT and Fe@MWCNT, iNOS mRNA was quantified as NO^{\bullet} producer in cells. Interestingly, iNOS mRNA was only increased in presence of Fe@MWCNT (Figure 5d) suggesting the ability of peroxynitrite to preferentially attack structural defect site constituted by the presence of iron. As MPO was described to take part in CNT degradation,¹¹ its mRNA expression was also quantified. Total mRNA for MPO was increased by 38% in treated cells compared to the control (Figure 5d), suggesting a possible implication of this protein in CNT degradation. Nevertheless, studies on

ROS produced by MPO in response to bacterial attack are mainly found in the extracellular matrix³⁶ indicating that MPO could be produced by cells to induce extracellular CNT degradation.

As sketched in Figure 6, macrophages employed several oxidative mechanisms to degrade CNTs outside and inside the cells. Particularly, our pluridisciplinary approach of MWCNT biodegradation in macrophages sheds light on a multistep process based on the phagocytosis of MWCNTs, the activation of NOX₂ complex into phagosomes with the purpose of producing ROS, leading to the chemical attack of the graphitic nanostructures by OH[•]. Furthermore, the implication of NOX₂ in the cell response to CNT allows highlighting many *in vitro* and *in vivo* studies on CNTs. NOX₂ complex need to be associated with Rac₂ protein for its activation. Rho-GDP dissociation inhibitor (Rho GDI) is a small protein associated to Rac₂-GDP in the cytoplasm.³⁷ To be activated and move from the cytoplasm to the membrane, Rac₂ changes his GDP to GTP. This modification leads to the dissociation of Rac₂ and Rho GDI explaining the induction of Rho GDI protein alone in cells. Hence the activation of NOX₂ complex demonstrated in this study could explain previous proteomic studies showing CNT- induced over-activity of Rho GDI.⁴⁰⁻⁴² Moreover, it was also established that CNTs could cause cytoskeleton protein variations in macrophages,^{41, 43} alveolar basal epithelial cells⁴⁰ or keratinocytes.⁴² Notably, Ju *et al.* demonstrated that MWCNTs increase the actin expression in A549 cells, but this effect is significantly attenuated by the inhibition of ROS by NAC.⁴⁰ These results are in line with the NAC-induced low activity of NOX₂ complex, because p47phox has the ability to influence cytoskeletal organization.⁴⁴ Our results are also supported by an *in vivo* study on knockout mice that cannot produce NOX_{2β}.⁴⁵ After a single instillation of 40 μg of SWCNTs in the lung, alveolar macrophages and neutrophils were found in larger numbers in the bronchoalveolar fluid of knockout mice compared to normal mice. This cell accumulation was associated with production

of pro-inflammatory cytokines (IL6, MCP-1, TNF) and suppression of the anti-inflammatory/pro-fibrotic response (TGF β) that are ordinarily induced by CNTs in mice that cannot clear them.⁴⁶⁻⁴⁸

In light of the present study, we could conclude that in the absence of NOX₂ β , CNTs could not be degraded and pro-inflammatory response was activated. In another study, Shvedova *et al.* have shown that vitamin E deficiency enhances pulmonary inflammatory response and oxidative stress induced by SWCNTs in mice.⁴⁹ Interestingly, a study performed on HIV-gp120 protein revealed the ability of vitamin E to regulate ROS generated by NOX₂ complex, supporting the role of NOX₂ complex in the degradation of CNTs and the role of pro-inflammatory cytokine as regulator of cell response to CNTs.

Conclusion

The biodegradation of MWCNTs in macrophages was investigated by simultaneously examining the influences of intracellular environment on the atomic structure of nanomaterials and probing the genetic responses of the cells to CNTs. Liquid-cell TEM was exploited for the first time to follow the dynamical chemical attack of MWCNTs by OH \cdot at the nanoscale, revealing two electron dose-dependent routes of degradation: fast tearing and perforation of the walls are enabled on reactive structural defects, while a continuous thinning of the walls occurs in a non-site-specific manner. These nanoscale observations provide a mechanistic understanding of the ROS-induced transformations of MWCNTs that could be exploited for drug delivery applications and for better controlling the life-cycle of CNTs in biological environments. The crucial role of NOX₂ complex in the biological pathway leading to a controlled production of ROS in the vicinity of MWCNTs and their subsequent degradation was clearly established. These intracellular transformations, together with the already revealed extra-cellular degradation of CNTs,¹⁶ emphasize on the various

oxidative mechanisms deployed by macrophages to process graphitic nanostructures. More generally, this interdisciplinary approach to study the reciprocal interactions between endogenous and exogenous species should be applied to others nanosystems and biological environments, because it provides crucial information for the development of efficient and safe nanomedicine.

Methods

Synthesis of MWCNTs and Fe@MWCNTs: MWCNTs were provided by Pyrograph Products (Cedarville, OH). Their inner diameter varies from 40 to 80 nm. As reported in previous study,¹⁷ to produce Fe@MWCNTs, MWCNTs were first washed with HNO₃ to remove traces of the residual iron growth catalyst. To remove the maximum number of oxygenated species on their surface they were heated at 900°C under an inert atmosphere for 4 h. The elimination of oxygenated groups at the surface of MWCNTs was confirmed by X-ray photoelectron spectroscopy.⁵⁰ MWCNTs were first dispersed in octadecene under ultrasonication. Iron stearate was then added, and the solution was heated at 120°C for 12 h to dissolve the reactants, to eliminate the traces of water or impurities, and to favor the diffusion of metal precursors inside MWCNTs. Then, the mixtures were heated at 318°C (heating rate 5°C/min) under air for 2 h. Finally, the products were washed four times with ethanol and chloroform, then centrifuged, followed by a conventional filtration method to remove NPs formed outside MWCNTs.⁵¹ After this first filling step, once the mixture was heated and cooled to room temperature, the same synthesis was repeated again without washing steps by adding iron stearate as a precursor.

Functionalization of MWCNTs and Fe@MWCNTs: MWCNTs and Fe@MWCNTs were functionalized by arylation to introduce amino groups on their sidewall and increase their dispersibility in water.¹⁷ Iron Mass Fraction was quantified in previous study¹⁷ by ICP-AES revealing the absence of iron for MWCNT and an iron mass fraction of 6.64% for Fe@MWCNT.

Preparation and characterization of MWCNT and Fe@MWCNT suspensions: Nanotubes were suspended in cell culture media at a concentration of 100 µg/ml. The suspensions were sonicated for 5 min (5s pause every 30s) at 60 W with an ultrasonic bath (sonorex digitec, Bandelin). The quality of the suspensions was visually estimated and agglomerates sizes were quantified using nanoparticle tracking analysis system (Nanosight, Malvern). Agglomerate mean size was quantified to be 114 ± 1.6 nm and 123.7 ± 1.5 nm for MWCNT and Fe@MWCNT, respectively. 90% of the agglomerates were smaller than 173 ± 2.8 nm and 194.7 ± 12.7 nm for MWCNT and Fe@MWCNT, respectively.

MWCNT for in vivo experiments: MWCNT_{vi} (product number: 636649) was purchased from Sigma -Aldrich (Lyon, France). These nanotubes were synthesized by Chemical Vapor Deposition method. Their diameter ranged from 20 to 50 nm and their length from 0.5 to 2 µm (data from the supplier).

Cells and cytotoxicity test: The human monocytic cell line THP-1 were obtained from ATCC (France) and cultured in fresh supplemented media (RPMI 1640 medium supplemented with 10% FCS (Gibco, France), 2 mM glutamine (Gibco, France), 100 U/ml penicillin, and 100 mg/ml streptomycin (Gibco, France)) at 37 °C and 5% CO₂. The THP-1 cells were maintained between 10^5 and 10^6 cells/ml in fresh supplemented RPMI media. In the exponential phase of growth, cells were seeded onto 96-well plates at 80,000 cells per well. After 48h phorbol myristate acetate

1
2
3
4
5
6
7
8
9
10
11
12
13
14
15
16
17
18
19
20
21
22
23
24
25
26
27
28
29
30
31
32
33
34
35
36
37
38
39
40
41
42
43
44
45
46
47
48
49
50
51
52
53
54
55
56
57
58
59
60

(PMA) treatment at 5 ng/ml, the cells were washed and exposed 24h to various concentrations of MWCNTs or Fe@MWCNTs (0, 0.53, 1.06, 3.12, 6.25, 12.5, 25, 50, 75, 100 µg/ml) in RPMI media. All the suspensions were prepared extemporary in tubes and 100 µl was added directly on the cells. The cell viability was determined 24h after treatment by Alamar blue[®] assay (Alamar blue[®] reagent, Biosource, France). At the end of the tests, optical density was measured on 80 µl supernatant transferred in another clean culture plate.

Oxidative stress assessment: Cells were seeded onto 96-well plates at 80,000 cells per well in presence of 5 ng/ml of PMA. After 48h, cells were washed and fresh supplemented media was added for 24h. Then, cells were pre-treated or not for 30 min with 10 mM of NAC and exposed to 5 µg/ml of MWCNTs or Fe@MWCNTs in the presence or absence of NAC. After 24h, cells were washed with PBS, loaded with 50 µM of 2,7-dichlorofluorescein diacetate (DCF-DA) for 40 min and washed again with PBS. After a further incubation in PBS for 1 h the fluorescence intensities were measured at 488 nm excitation and 530 nm emission in the fluorescence plate reader (Fluostar Galaxy CTC 435,BMG).

Animals: Male Sprague-Dawley rats weighing 180–220 g were purchased from Charles River Laboratories (St Germain-sur-l’Arbresle, France). The rats were kept in a conventional animal facility and had access ad libitum to food and drink. The experimental protocol has been approved by the local ethical committee for animal research.

TEM experiments: All the *in situ* and *in vitro* TEM experiments were realized on the JEOL ARM 200F microscope equipped together with a CEOS aberration corrector for the objective lens and a cold FEG. All the experiments were performed with an 80 kV acceleration voltage.⁵²

TEM structural analyses of MWCNTs and Fe@MWCNTs after aging in THP-1-derived macrophages : Cells were seeded onto 75 cm² flasks at 12×10^6 cells per flask in presence of 5 ng/ml of PMA. After 48h, cells were washed and fresh supplemented media was added for 24 h. Then, cells were pre-treated or not for 30 min with 10 mM of NAC and exposed to 5 µg/ml of MWCNTs or Fe@MWCNTs in the presence or absence of NAC. After 24h incubation time, cells were washed with PBS and fresh supplemented media was added in order to remove the non-phagocytized nanomaterials. Three hours, 24h, 48h or 168h after exposure, cells were scraped and a centrifugation step at 350g for 10 min was performed to separate the cells from the media. Cells were suspended in presence of 200 µl of distilled water in a sonication bath at maximum power for 1 min, to lyse them by osmotic shock. Cell lysate was then centrifuged at 10,000g for 5 min. Supernatant was eliminated by pipetting and the pellet containing MWCNTs and cell residues was dispersed in water. After a final heating step at 80°C for 15 min to remove the last cell residues, 10 µl of the suspensions was deposited on carbon TEM grid and then dried for 5 min before TEM and HRTEM observations. To confirm that this extraction procedure did not affect the structure of the MWCNTs a control sample was realized on 3 ml of suspension used to expose the cells. To compare MWCNTs extracted from cells and MWCNTs from control both heating (37°C for 3h to 168h aging time; 80°C for 15 min) and centrifugation steps (350g for 5 min and 10,000g for 5 min) were performed on the suspension in absence of cells. TEM analysis of this control sample revealed that the structure of MWCNTs is not disturbed by the extraction procedure.

Liquid-cell sample preparation: The liquid cells commercialized by Protochips Inc. consist of two silicon wafers with dimensions of 2×2 mm and 4.5×6 mm, called the small and large E-chips, respectively (Figure S9). Each E-chip has one 550 µm × 50 µm window covered by a 30 nm thick silicon-nitrite amorphous film. A 2.5 µL drop of MWCNT or Fe@MWCNT suspension dispersed

in water or in ethanol, was deposited on the electron transparent membrane of the small E-chip. The large E-chip was then placed over the small one with their windows in cross-configuration, giving a square field of view of 50 μm edge length. Therefore, the drop of solution was squeezed in between the two E-chips in a volume defined by the thickness of the gold spacers on the small E-chip (150 nm in our case). The entire chamber was then closed by the lid of the holder tip resulting in a vacuum sealed liquid-cell. As illustrated in Figure S9, the impermeability of the liquid cell is ensured by two concentric O-rings. We did not use the holder in flow mode. The thickness of the spacers corresponds to the smallest liquid thickness crossed by the electron beam during the TEM experiment. Indeed due to the outward bowing of the SiN membranes under vacuum, the smallest liquid thickness is found at the corners of the viewing window. All the images were recorded close to the corners for improving signal to noise ratio.

In situ STEM imaging: STEM HAADF imaging was performed without changing probe size (5C) and condenser aperture (70 μm) in order to maintain a constant beam current (i_e). The latter was measured on the phosphorescent screen of the microscope prior to insert the sample to determine the dose rate focalized on the liquid cell ($i_e = 3.74 \times 10^8$ electron/s or 59.8 pA). MWCNT degradation was followed by continuously recording 512 \times 512 images with a pixel dwell time of 5 μs . In electron microscopy the dose rate (\dot{d}) is usually calculated in electrons/ $\text{\AA}^2\text{s}$ by dividing i_e by the surface irradiated by the beam, which in STEM mode advantageously corresponds to the imaged area. Therefore, \dot{d} was easily controlled since it is inversely proportional to the square of the magnification. With such optical conditions, \dot{d} varies from 4.5 to 32 electrons/ $\text{\AA}^2\text{s}$, with the magnification used for imaging (from 150k to 400k). The conversion of \dot{d} in $\text{Gy}\cdot\text{s}^{-1}$ (*i.e.* $\text{J}\cdot\text{kg}^{-1}\cdot\text{s}^{-1}$), units commonly used in the field of radiation chemistry, simply requires multiplying \dot{d} in electron/ $\text{m}^2\cdot\text{s}$ by the density normalized stopping power of the solvent (4.761×10^5 and 4.961×10^5

1
2
3 eV·m²/kg per electron, at 80 kV for water and ethanol, respectively) and by 1.6 10⁻¹⁹ to convert
4
5 electron-volts to joules. This leads to \dot{d} in between 3.4×10⁷ and 2.4 10⁸ Gy·s⁻¹ for magnification
6
7 ranging from 150k to 400k in water. \dot{d} is slightly more important in ethanol for equivalent optical
8
9 conditions.
10
11

12
13
14 **Cytotoxicity of degradation products:** 24h after exposure, MWCNTs or Fe@MWCNTs were
15
16 extracted from cells (see extraction procedure above), the degraded MWCNTs and Fe@MWCNTs
17
18 were suspended in 100 µl of distilled water. The concentrations of the dMWCNT and
19
20 dFe@MWCNT suspensions were then quantified using DO₂₇₃ quantification method⁵³ against a
21
22 standard range of MWCNTs or Fe@MWCNTs. Cytotoxicity tests were then performed by Alamar
23
24 blue assay for different concentration of dMWCNT and dFe@MWCNT following the same
25
26 procedure than for MWCNTs and Fe@MWCNTs (see procedure above)
27
28
29
30

31
32 **In vivo degradation of MWCNT assessment:** 3 rats were exposed to 100 µg of MWCNT by
33
34 intratracheal instillation. 7 days after the exposure, the animals were anesthetized. The lungs and
35
36 the lymph nodes were removed, cut in small sections and fixed with 2.5% glutaraldehyde. After a
37
38 postfixation with 1% osmium tetroxide, the samples were dehydrated by ethanol and embedded in
39
40 EPON 812 (TAAB). The ultrathin sections of 90 nm and 150 nm respectively for TEM analyses
41
42 were obtained by an ultramicrotome (UCT, Leica), mounted on copper grids and stained with
43
44 uranyl acetate and examined in a Tecnai G₂ Biotwin (FEI) electron microscope using an
45
46 accelerating voltage of 100 kV. Several photographs of MWCNT_{vi} detailed structures were taken
47
48 analyzed and compared to control samples.
49
50
51
52

53
54 **NOX₂ complex and antioxidant protein markers by reverse transcription real time**
55
56 **polymerase chain reaction (RT-qPCR):** Cells were seeded onto 6-well plates at 2×10⁶ cells per
57
58
59
60

1
2
3
4
5
6
7
8
9
10
11
12
13
14
15
16
17
18
19
20
21
22
23
24
25
26
27
28
29
30
31
32
33
34
35
36
37
38
39
40
41
42
43
44
45
46
47
48
49
50
51
52
53
54
55
56
57
58
59
60

well in presence of 5 ng/ml of PMA. After 48h, cells were washed and fresh supplemented media was added for 24h. Then, cells were pre-treated or not for 30 min with 10 mM of NAC and exposed to 5 µg/ml of MWCNTs or Fe@MWCNTs in presence or absence of NAC. After 24h, cells were washed with PBS and total RNA was extracted from 10⁶ cells with NucleoSpin RNA II[®] Kit (Macherey Nagel) according to manufacturer’s protocol. One µg of total RNA was reverse transcribed to cDNA with SuperScript[®] Reverse Transcriptase (Invitrogen, Cat n°18064-014) according to the manufacture’s protocol using Random primer (Promega, Cat n°C1181) and RNasin (Promega, Cat n°N2511). The quantification of mRNA for RPL19 (housekeeping gene, Fwd 5’-TCATCAAAGATGGGCTGATCAT-3’; Rev 5’-CATCGAGCCCGGGAATG-3’); NOX_{2α} (Fwd 5’-GGGCCCTTTACCAGGAATTACT-3’; Rev 5’-GGCACCGAGAGCAGGAGAT-3’); NOX_{2β} (Fwd 5’-TGTGTGAATGCCCCGAGTCAA-3’; Rev 5’-TACAGGCCTCCTTCAGGGTT-3’); p47phox (Fwd 5’-CCCATCATCCTGCAGACGTA-3’; Rev 5’-GAGCCCGAGGTCTTCTCGTA-3’); p40phox (Fwd 5’-AGCTCACAAGGCGGGAGTT-3’; Rev 5’-TCAGCGTCCCGGTAATTCAG-3’); p67phox (Fwd 5’-GCCCAGACATTCCAAAATCG-3’; Rev 5’-GGCTCATATAGCTTCTGCTTCCA-3’); MPO (Fwd 5’-GCCAAGCTGAATCGTCAGAAC-3’; Rev 5’-TCATGACCTGCTCAAACAATCG-3’); SOD-Cu (Fwd 5’-CAGGGCATCATCAATTTCTGA-3’; Rev 5’-TGCTTCCCCACACCTTCAC-3’); SOD-Mn (Fwd 5’-CGCGGCCTACGTGAACA-3’; Rev 5’-CCAACGCCTCCTGGTACTTC-3’); GSTP1 (Fwd 5’-CGGGCAACTGAAGCCTTTT-3’; Rev 5’-AAGGTCTTGCCTCCCTGGTT-3’); Ferritin L (Fwd 5’-CGAATTGGCCGAGGAGAA-3’; Rev 5’-GCCACGCTGGTTTTGCAT-3’); Ferritin H (Fwd 5’-TGGCTTGGCGGAATTTCTGT-3’; Rev 5’-GCCCCGAGGCTTAGCTTTTCAT-3’); iNOS (Fwd 5’-CCCCTTCAATGGCTGGTACA-3’; Rev 5’-GCGCTGGACGTCACAGAA-3’)

transcript were performed using SYBR® green PCR master Mix (Applied Biosystems, Cat n°4367659) according to the manufacturer's protocol on 300 ng of cDNA using StepOne plus Mastercycler (Applied Biosystems). Each sample was run in duplicate.

Protein quantification performed by western blot analysis: Cells were seeded onto 6-well plates at 2×10^6 cells per well in presence of 5 ng/ml of PMA. After 48h, cells were washed and fresh supplemented media was added for 24h. Then, cells were pre-treated or not for 30 min with 10 mM of NAC and exposed to 5 μ g/ml of MWCNTs or Fe@MWCNTs in presence or absence of NAC. After 24h, cells were washed with PBS and proteins were extracted with Nucler/Cytosol fractionation Kit (Biovision) according to manufacturer's protocol. Presence of NOX₂ β and Ferritin H were analyzed on 50 μ g of cytosolic protein by SDS-PAGE (4-20% polyacrylamide, Mniprotean TGX, Biorad). Separated proteins were transferred onto nitrocellulose membranes. Blots were saturated 1h in TBST (Tris-base, pH 7.4, Tween 20 %)-5% BSA and washed in TBST (3x5 min). They were subsequently incubated for 2 h with a rabbit NOX₂ β or Ferritin H antibody (Santa Cruz) diluted at 1:300 in TBST-BSA 3%. After washing in TBST (3x5 min), the membranes were reacted with a goat anti-rabbit-HRP antibody (Santa Cruz) diluted at 1:3300 in TBST-BSA 3%. Presence of proteins was visualized with a chemiluminescent system (ECL+ Western blot detection kit, Amersham). Densitometry of each condition was calculated using ImagJ software. To compare the effect of each treatment, a R_d ratio was calculated as follow:

$$R_d = \frac{D_{ex1} \times D_{con2}}{D_{ex2} \times D_{con1}}$$

Where D_{ex1} , D_{ex2} are the densities of exposed groups for NOX₂ β (or FerH) and RPL19 and D_{con1} and D_{con2} are the densities of control groups for NOX₂ β (or FerH) and RPL19.

1
2
3
4
5
6
7
8
9
10
11
12
13
14
15
16
17
18
19
20
21
22
23
24
25
26
27
28
29
30
31
32
33
34
35
36
37
38
39
40
41
42
43
44
45
46
47
48
49
50
51
52
53
54
55
56
57
58
59
60

Statistics: All data were expressed as mean \pm S.D (standard deviation). F-test was used to compare the homogeneity of the variances. If homogeneity of variance was verified with a risk alpha equal to 5 %, differences between each group were assessed with a one-way analysis of variance (ANOVA). When all ANOVA tests were positive, groups were subjected to the multiple-comparison Dunnett's test. If the variances were not homogeneous, no significant differences between groups were considered. * $P < 0.05$ was considered as the statistical significance level. For each aging time point 3h, 24h, 48h, 168h of CNTs in cells in presence or absence of NAC, percentage of perforated area (P_a), the mean surface area of holes (\bar{S}) and the density of holes (D) were measured in MWCNTs and Fe@MWCNTs. Hole surface areas at each time point could be assimilated as a distribution and then compared per pair using Kolmogorov Smirnov test. P-values obtained by Kolmogorov-Smirnov test which are less than 0.05 show significant differences between the two distributions.

FIGURES

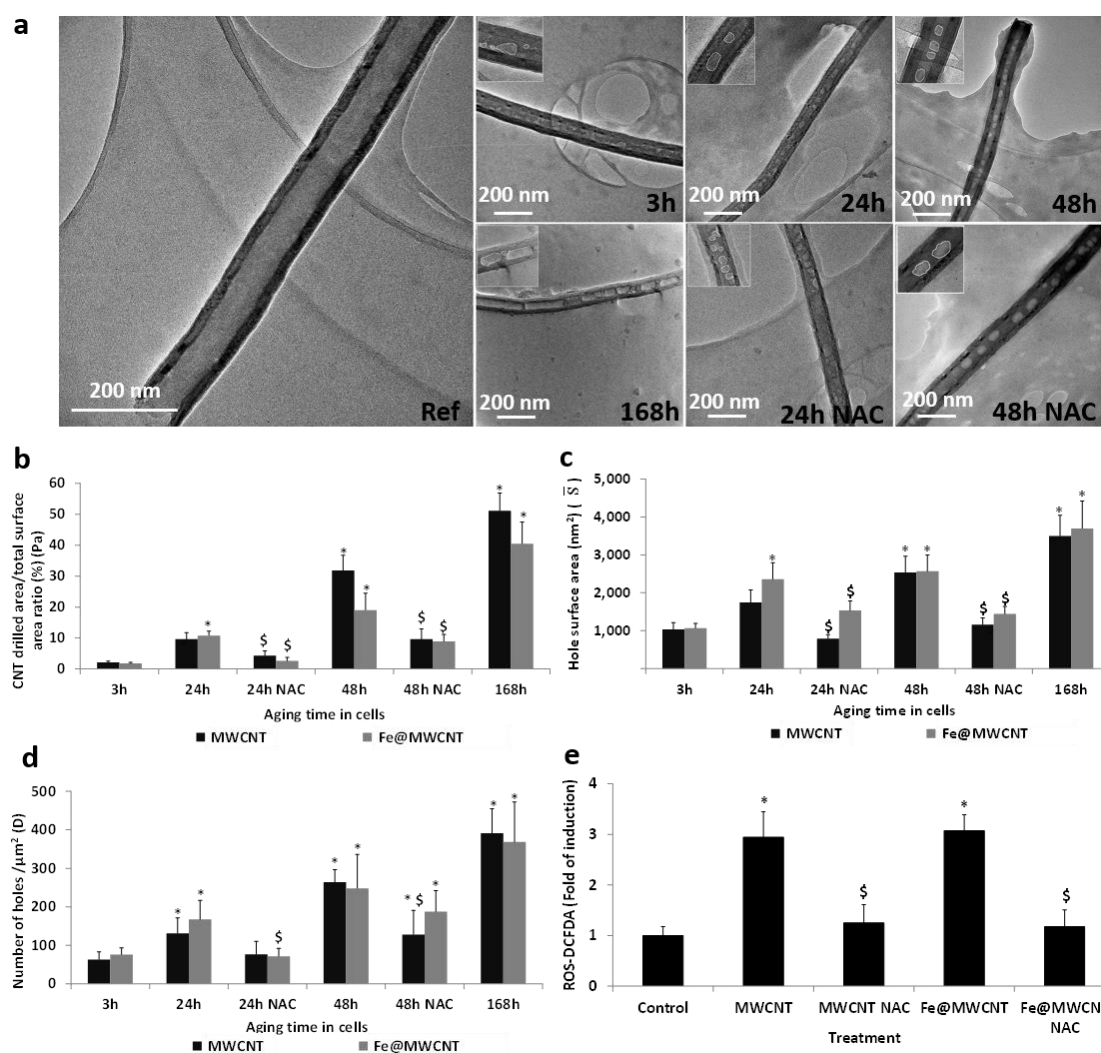


Figure 1. MWCNT and Fe@MWCNT degradation in THP-1 differentiated into macrophages. a, TEM observations of MWCNTs before (Ref) and after aging into cells. The aging time and the presence of NAC in cells are indicated in the bottom right corner of each image. b, Ratio of total perforated area to total surface area (P_a), c, mean surface area of holes (\bar{S}) and d, density of holes (D) in MWCNTs or Fe@MWCNTs as a function of the aging time in cells and the presence or absence of NAC. e, Formation of ROS in THP-1 after treatment with a 5 $\mu\text{g/ml}$ suspension of MWCNTs or Fe@MWCNTs for 24 h. ROS were detected by fluorescence measurement of the DCFDA reporter and results are given in fold of untreated controls. Data shown in panels b, c and d are from three independent experiments (minimum 50 observed items) and are expressed as mean values \pm S.D. Results in panel e are the mean \pm SD of 3 separate experiments, each carried in triplicates. (*) Designates a statistically-significant difference from 3h group ($p < 0.05$) (panel b, c and d) or control group (panel e). (\$) Designates a statistically-significant difference between MWCNT NAC or Fe@MWCNT NAC groups and its respective equivalent MWCNT or Fe@MWCNT group without NAC treatment ($p < 0.05$).

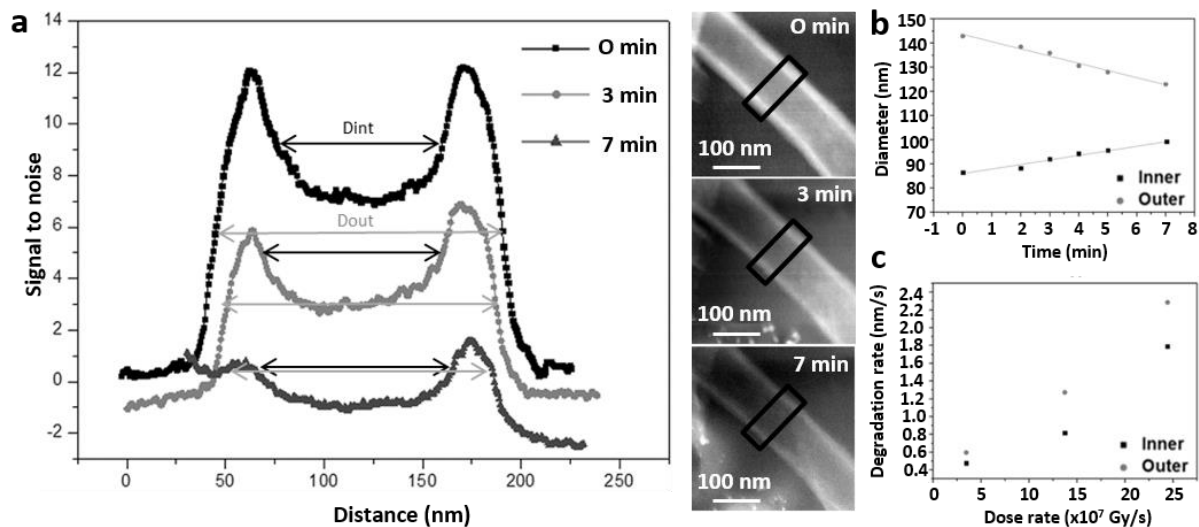


Figure 2. *In situ* liquid TEM in water. Dose-dependent thinning of MWCNTs due to OH• produced by radiolysis. a, Time evolution of signal-to-noise ratio (SNR) profile measured across a MWCNT, during non-site-specific degradation. The position and the width (100 nm) of the SNR profiles are indicated on the three STEM-HAADF images acquired at 400k magnification (corresponding dose rate of 2.4×10^8 Gy.s⁻¹, see method section) after 0, 3 and 7 min of irradiation. The inner (D_{int}) and outer (D_{out}) diameters were measured by considering the position of the sidewalls as the half maximum of the corresponding peaks on the SNR profiles. b, Time evolution of the inner and outer diameters of the MWCNT degraded in (a). The concomitant increase of the inner diameter and decrease of the outer diameter reveal that degradation occurs inside and outside of the MWCNTs. Linear regressions were applied to the size evolution of inner and outer diameters as a function of time, from which the slope corresponds to their kinetic of degradation. c, Degradation rate (nm/s) of the inner and outer diameters of CNT as a function of the electron dose given in Gy.s⁻¹ (see Methods).

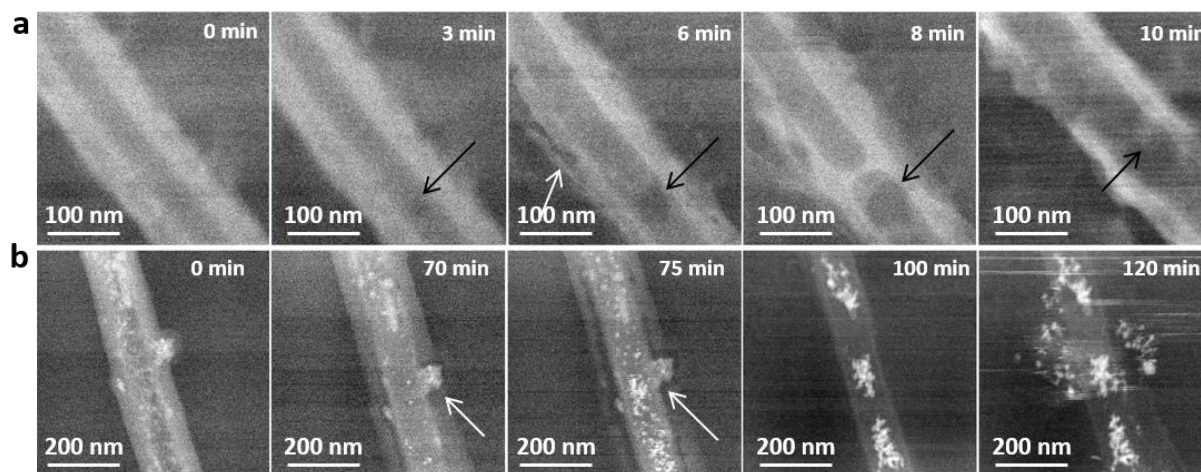


Figure 3. *In situ* liquid TEM in water. Site-specific drilling of MWCNTs induced by OH• chemical attack. Time series of STEM-HAADF images with the observation time indicated in the top right corner of each image. a, Drilling process in a MWCNT acquired with a magnification of 400k (corresponding dose rate of $2.4 \times 10^8 \text{ Gy.s}^{-1}$, see method section). Black arrows indicate the nucleation and growth of a spherical hole and the white arrow shows a tearing of the nanotube along the anisotropy axis. A video file of this image series accelerated 16 times can be seen in supplementary. b Drilling process in a Fe@MWCNT acquired with a magnification of 200k (corresponding dose rate of $6 \times 10^7 \text{ Gy.s}^{-1}$, see Method). White arrows show a tearing of the nanotube along the interface between the graphitic structure and the iron oxide nanoparticles inserted in the carbon walls.

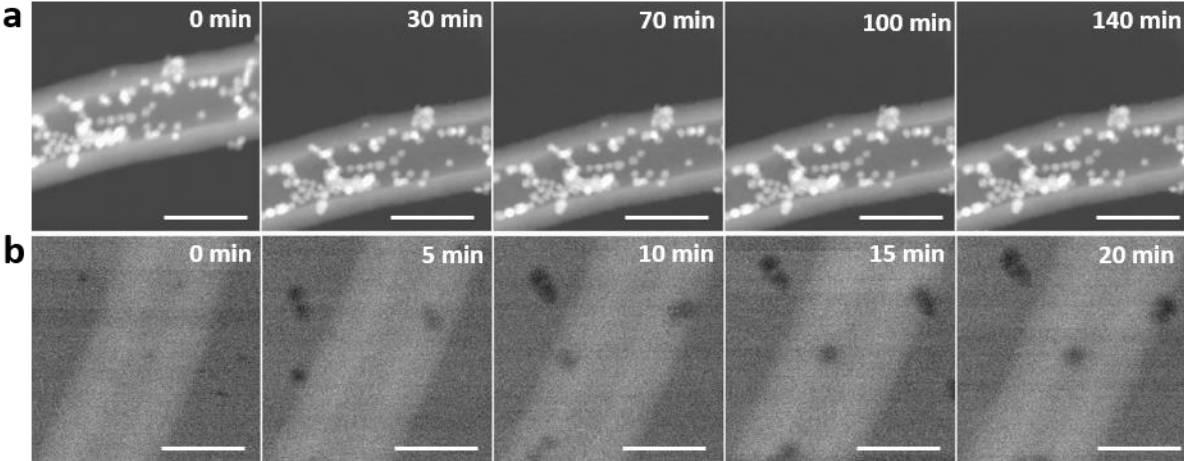


Figure 4: *Stability of MWCNTs and Fe@MWCNTs under similar beam irradiation conditions in vacuum and in ethanol.* STEM HAADF image series acquired at 80 kV with a magnification of 400k. The observation time on the analyzed area is indicated in the top right corner of each image. **a**, No degradation of Fe@MWCNTs is observed under vacuum condition (conventional STEM observation) revealing the absence of knock-on damage induced by electron beam. **b**, No degradation of MWCNTs is observed in ethanol in which the electron beam creates peroxy groups but no OH[•] (circular black contrasts are imaging artefacts). Scale bars correspond to 100 nm in each image

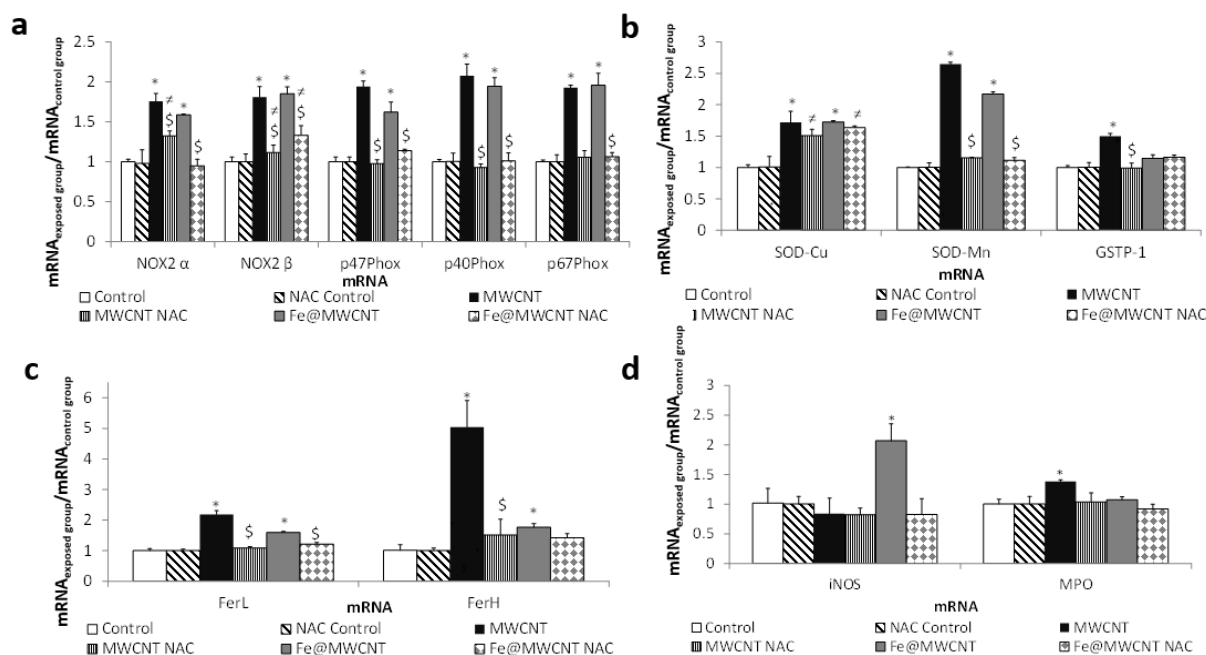


Figure 5. Effect of MWCNTs and Fe@MWCNTs on the gene expression level of NOX₂ complex and antioxidant proteins. THP-1 cells were treated with 5 μ g/ml of MWCNT or Fe@MWCNT suspension. After 24h exposure, mRNA quantification of a, NOX2 α , NOX2 β , p47phox, p40phox, and p67phox; b, SOD-Cu, SOD-Mn and GSTP1; c, Ferritin L and Ferritin H; and d, INOS and MPO. Results are the mean \pm SD of 3 separate experiments. (*) Designates a statistically-significant difference from control group ($p < 0.05$). (\$) Designates a statistically-significant difference between MWCNTs NAC or Fe@MWCNT NAC group and its respectively equivalent MWCNTs or Fe@MWCNTs group without NAC treatment ($p < 0.05$). (≠) Designates a statistically-significant difference between MWCNT NAC or Fe@MWCNTs NAC and NAC control group ($p < 0.05$).

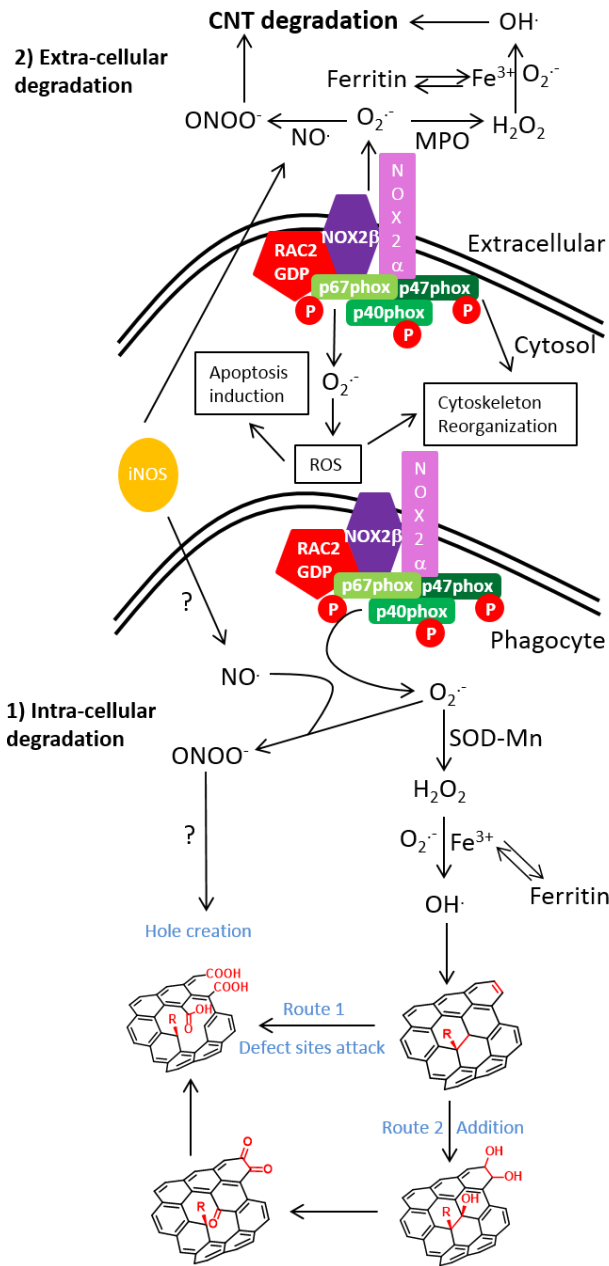


Figure 6. Schematic representation of the biological pathways of MWCNT degradation in macrophages. 1) Intracellular oxidative degradation: After engulfment of MWCNTs, NOX₂ complex is activated on cytosolic and phagosomal membranes. Active NOX₂ complex induced O₂^{•-} production and then cytoskeleton reorganization. Into phagosome, O₂^{•-} is turned into H₂O₂ by SOD and H₂O₂ is turned in presence of Fe³⁺ into OH[•] (Haber-Weiss reaction). OH[•] could attack MWCNT defects and unsaturated carbon bonds on the sidewalls of CNTs to generate carboxylic acids creating holes in the graphitic structure. 2) Extracellular oxidative degradation: MWCNT outside the cells can also be degraded by two routes: (i) Production of OH[•] via NOX₂ complex and MPO, or (ii) Peroxynitric attack as described by kagan et al.¹⁶

ASSOCIATED CONTENT

Supporting Information. Supplementary figures and a video accelerated 16 times of nanotube degradation in water (corresponding to figure 3a) are available free of charge *via* the Internet at <http://pubs.acs.org>.”

AUTHOR INFORMATION

Corresponding Author

* Damien Alloyeau: alloyeau.damien@gmail.com and Florence Gazeau : florence.gazeau@univ-paris-diderot.fr

Author Contributions

‡These authors contributed equally.

ACKNOWLEDGMENT

This work was supported by the CNRS (Centre National de la Recherche Scientifique, Defi Nano program), the ANR (Agence Nationale de la Recherche) and CGI (Commissariat à l'Investissement d'Avenir) through the LabEx SEAM (Science and Engineering for Advanced Materials and devices; ANR 11 LABX 086, ANR 11 IDEX 05 02) and the LabEx Chemistry of Complex Systems (ANR-10-LABX-0026_CSC), by the ANR project DECANO (ANR-2011-CESA-007-01) and by the International Center for Frontier Research in Chemistry (icFRC).

REFERENCES

1. Lanone, S.; Boczkowski, J. Biomedical Applications and Potential Health Risks of Nanomaterials: Molecular Mechanisms. *Curr Mol Med* **2006**, 6, 651-63.
2. Sechi, G.; Bedognetti, D.; Sgarrella, F.; Van Eperen, L.; Marincola, F. M.; Bianco, A.; Delogu, L. G. The Perception of Nanotechnology and Nanomedicine: A Worldwide Social Media Study. *Nanomedicine* **2014**, 9, 1475-86.
3. Elgrabli, D.; Floriani, M.; Abella-Gallart, S.; Meunier, L.; Gamez, C.; Delalain, P.; Rogerieux, F.; Boczkowski, J.; Lacroix, G. Biodistribution and Clearance of Instilled Carbon Nanotubes in Rat Lung. *Part Fibre Toxicol.* **2008**, 5, 20.
4. McDevitt, M. R.; Chattopadhyay, D.; Kappel, B. J.; Jaggi, J. S.; Schiffman, S. R.; Antczak, C.; Njardarson, J. T.; Brentjens, R.; Scheinberg, D. A. Tumor Targeting with Antibody-Functionalized, Radiolabeled Carbon Nanotubes. *J Nucl Med* **2007**, 48, 1180-1189.
5. Wang, H.; Wang, J.; Deng, X.; Sun, H.; Shi, Z.; Gu, Z.; Liu, Y.; Zhao, Y. Biodistribution of Carbon Single-Wall Carbon Nanotubes in Mice. *J Nanosci Nanotechnol* **2004**, 4, 1019-24.
6. Shvedova, A. A.; Kisin, E. R.; Mercer, R.; Murray, A. R.; Johnson, V. J.; Potapovich, A. I.; Tyurina, Y. Y.; Gorelik, O.; Arepalli, S.; Schwegler-Berry, D., *et al.* Unusual Inflammatory and Fibrogenic Pulmonary Responses to Single-Walled Carbon Nanotubes in Mice. *Am J Physiol Lung Cell Mol Physiol* **2005**, 289, L698-708.
7. Flaviu, T.; Catoi, C.; Mocan, T.; Mocan, L.; Biris, A.; Simon, S.; Nagy, A.; Taulescu, M.; BolfĂ, P.; Catoi, A. F. Interaction between Kupffer Cells and Carbon Nanotubes-Transition from Biodistribution and Toxicity to Kupffer Cell Targeted Therapy. *Bulletin of the University of Agricultural Sciences & Veterinary Medicine Cluj-Napoca. Veterinary Medicine* **2013**, 70, 147.
8. Lacerda, L.; Ali-Boucetta, H.; Herrero, M. A.; Pastorin, G.; Bianco, A.; Prato, M.; Kostarelos, K. Tissue Histology and Physiology Following Intravenous Administration of Different Types of Functionalized Multiwalled Carbon Nanotubes. *Nanomedicine* **2008**, 3, 149-61.
9. Cherukuri, P.; Bachilo, S. M.; Litovsky, S. H.; Weisman, R. B. Near-Infrared Fluorescence Microscopy of Single-Walled Carbon Nanotubes in Phagocytic Cells. *J. Am. Chem. Soc.* **2004**, 126, 15638-15639.
10. Allen, B. L.; Kichambare, P. D.; Gou, P.; Vlasova, II; Kapralov, A. A.; Konduru, N.; Kagan, V. E.; Star, A. Biodegradation of Single-Walled Carbon Nanotubes through Enzymatic Catalysis. *Nano Lett* **2008**, 8, 3899-903.
11. Kagan, V. E.; Konduru, N. V.; Feng, W.; Allen, B. L.; Conroy, J.; Volkov, Y.; Vlasova, II; Belikova, N. A.; Yanamala, N.; Kapralov, A., *et al.* Carbon Nanotubes Degraded by Neutrophil Myeloperoxidase Induce Less Pulmonary Inflammation. *Nat Nanotechnol* **2010**, 5, 354-9.
12. Andon, F. T.; Kapralov, A. A.; Yanamala, N.; Feng, W.; Baygan, A.; Chambers, B. J.; Hultenby, K.; Ye, F.; Toprak, M. S.; Brandner, B. D., *et al.* Biodegradation of Single-Walled Carbon Nanotubes by Eosinophil Peroxidase. *Small* **2013**, 9, 2721-2729.
13. Bhattacharya, K.; El-Sayed, R.; Andón, F. T.; Mukherjee, S. P.; Gregory, J.; Li, H.; Zhao, Y.; Seo, W.; Fornara, A.; Brandner, B., *et al.* Lactoperoxidase-Mediated Degradation of Single-Walled Carbon Nanotubes in the Presence of Pulmonary Surfactant. *Carbon* **2015**, 91, 506-517.

14. Farrera, C.; Bhattacharya, K.; Lazzaretto, B.; Andon, F. T.; Hultenby, K.; Kotchey, G. P.; Star, A.; Fadeel, B. Extracellular Entrapment and Degradation of Single-Walled Carbon Nanotubes. *Nanoscale* **2014**, 6, 6974-83.
15. Russier, J.; Ménard-Moyon, C.; Venturelli, E.; Gravel, E.; Marcolongo, G.; Meneghetti, M.; Doris, E.; Bianco, A. Oxidative Biodegradation of Single- and Multi-Walled Carbon Nanotubes. *Nanoscale* **2011**, 3, 893-6.
16. Kagan, V. E.; Kapralov, A. A.; St Croix, C. M.; Watkins, S. C.; Kisin, E. R.; Kotchey, G. P.; Balasubramanian, K.; Vlasova, I.; Yu, J.; Kim, K., *et al.* Lung Macrophages "Digest" Carbon Nanotubes Using a Superoxide/Peroxynitrite Oxidative Pathway. *ACS Nano* **2014**, 8, 5610-21.
17. Liu, X.; Marangon, I.; Melinte, G.; Wilhelm, C.; Ménard-Moyon, C.; Pichon, B. P.; Ersen, O.; Aubertin, K.; Baaziz, W.; Pham-Huu, C., *et al.* Design of Covalently Functionalized Carbon Nanotubes Filled with Metal Oxide Nanoparticles for Imaging, Therapy, and Magnetic Manipulation. *ACS Nano* **2014**, 8, 11290-304.
18. Kagan, V. E.; Tyurina, Y. Y.; Tyurin, V. A.; Konduru, N. V.; Potapovich, A. I.; Osipov, A. N.; Kisin, E. R.; Schwegler-Berry, D.; Mercer, R.; Castranova, V., *et al.* Direct and Indirect Effects of Single Walled Carbon Nanotubes on Raw 264.7 Macrophages: Role of Iron. *Toxicol Lett* **2006**, 165, 88-100.
19. Panasenkov, O. M.; Chekanov, A. V.; Arnhold, J.; Sergienko, V. I.; Osipov, A. N.; Vladimirov, Y. A. Generation of Free Radicals During Decomposition of Hydroperoxide in the Presence of Myeloperoxidase or Activated Neutrophils. *Biochemistry (Mosc)* **2005**, 70, 998-1004.
20. Zhao, Y.; Allen, B. L.; Star, A. Enzymatic Degradation of Multiwalled Carbon Nanotubes. *J Phys Chem A* **2011**, 115, 9536-44.
21. de Jonge, N.; Ross, F. M. Electron Microscopy of Specimens in Liquid. *Nat Nanotechnol* **2011**, 6, 695-704.
22. Williamson, M. J.; Tromp, R. M.; Vereecken, P. M.; Hull, R.; Ross, F. M. Dynamic Microscopy of Nanoscale Cluster Growth at the Solid-Liquid Interface. *Nat Mater* **2003**, 2, 532-6.
23. Woehl, T. J.; Jungjohann, K. L.; Evans, J. E.; Arslan, I.; Ristenpart, W. D.; Browning, N. D. Experimental Procedures to Mitigate Electron Beam Induced Artifacts During in Situ Fluid Imaging of Nanomaterials. *Ultramicroscopy* **2013**, 127, 53-63.
24. Schneider, N. M.; Norton, M. M.; Mendel, B. J.; Grogan, J. M.; Ross, F. M.; Bau, H. H. Electron-Water Interactions and Implications for Liquid Cell Electron Microscopy. *The Journal of Physical Chemistry C* **2014**, 118, 22373-22382.
25. De Clercq, A.; Dachraoui, W.; Margeat, O.; Pelzer, K.; Henry, C. R.; Giorgio, S. Growth of Pt-Pd Nanoparticles Studied in Situ by Hrtm in a Liquid Cell. *The Journal of Physical Chemistry Letters* **2014**, 5, 2126-2130.
26. Evans, J. E.; Jungjohann, K. L.; Browning, N. D.; Arslan, I. Controlled Growth of Nanoparticles from Solution with in Situ Liquid Transmission Electron Microscopy. *Nano Lett* **2011**, 11, 2809-13.
27. Zheng, H.; Smith, R. K.; Jun, Y. W.; Kisielowski, C.; Dahmen, U.; Alivisatos, A. P. Observation of Single Colloidal Platinum Nanocrystal Growth Trajectories. *Science* **2009**, 324, 1309-12.
28. Alloeyau, D.; Dachraoui, W.; Javed, Y.; Belkahla, H.; Wang, G.; Lecoq, H.; Ammar, S.; Ersen, O.; Wisnet, A.; Gazeau, F., *et al.* Unravelling Kinetic and Thermodynamic Effects on the

- Growth of Gold Nanoplates by Liquid Transmission Electron Microscopy. *Nano Lett* **2015**, 15, 2574–2581.
29. Liao, H. G.; Niu, K.; Zheng, H. Observation of Growth of Metal Nanoparticles. *Chem Commun (Camb)* **2013**, 49, 11720-7.
30. Zhao, Y.; Burkert, S. C.; Tang, Y.; Sorescu, D. C.; Kapralov, A. A.; Shurin, G. V.; Shurin, M. R.; Kagan, V. E.; Star, A. Nano-Gold Corking and Enzymatic Uncorking of Carbon Nanotube Cups. *J Am Chem Soc* **2015**, 137, 675-84.
31. Gardes-Albert, M.; Bonnefont-Rousselot, D.; Abedinzadeh, Z.; Jore, D. Reactive Oxygen Species. How Oxygen May Become Toxic? *L'Actualité chimique* **2003**, 11, 91-96.
32. Li, W.; Bai, Y.; Zhang, Y.; Sun, M.; Cheng, R.; Xu, X.; Chen, Y.; Mo, Y. Effect of Hydroxyl Radical on the Structure of Multi-Walled Carbon Nanotubes. *Synthetic Metals* **2005**, 155, 509-515.
33. Amiri, A.; Memarpoor-Yazdi, M.; Shanbedi, M.; Eshghi, H. Influence of Different Amino Acid Groups on the Free Radical Scavenging Capability of Multi Walled Carbon Nanotubes. *Journal of Biomedical Materials Research Part A* **2013**, 101A, 2219-2228.
34. Shieh, Y.-T.; Wang, W.-W. Radical Scavenging Efficiencies of Modified and Microwave-Treated Multiwalled Carbon Nanotubes. *Carbon* **2014**, 79, 354-362.
35. Shukla, P. K.; Mishra, P. C. Effects of Diameter, Length, Chirality and Defects on the Scavenging Action of Single-Walled Carbon Nanotubes for Oh Radicals: A Quantum Computational Study. *Chemical Physics* **2010**, 369, 101-107.
36. Dupre-Crochet, S.; Erard, M.; Nubetae, O. Ros Production in Phagocytes: Why, When, and Where? *J Leukoc Biol* **2013**, 94, 657-70.
37. Guichard, C.; Pedruzzi, E.; Fay, M.; Ben Mkaddem, S.; Coant, N.; Daniel, F.; Ogier-Denis, E. The Nox/Duox Family of Ros-Generating Nadph Oxidases. *Med Sci (Paris)* **2006**, 22, 953-9.
38. Pacher, P.; Beckman, J. S.; Liaudet, L. Nitric Oxide and Peroxynitrite in Health and Disease. *Physiol Rev* **2007**, 87, 315-424.
39. Szabo, C.; Ischiropoulos, H.; Radi, R. Peroxynitrite: Biochemistry, Pathophysiology and Development of Therapeutics. *Nat Rev Drug Discov* **2007**, 6, 662-80.
40. Ju, L.; Zhang, G.; Zhang, X.; Jia, Z.; Gao, X.; Jiang, Y.; Yan, C.; Duerksen-Hughes, P. J.; Chen, F. F.; Li, H., *et al.* Proteomic Analysis of Cellular Response Induced by Multi-Walled Carbon Nanotubes Exposure in A549 Cells. *PLoS One* **2014**, 9, e84974.
41. Shen, Z. L.; Nie, H. Y.; Wang, H. F.; Yang, B.; Zhong, L. J.; Zou, X. J.; Lou, Y. X.; Liu, D.; Guo, J.; Jia, G. Two Types of Mwnts with Different Surface Modifications Induce Differential Expression of Proteins in Raw264.7 Cells. *Beijing Da Xue Xue Bao* **2010**, 42, 345-50.
42. Witzmann, F. A.; Monteiro-Riviere, N. A. Multi-Walled Carbon Nanotube Exposure Alters Protein Expression in Human Keratinocytes. *Nanomedicine* **2006**, 2, 158-68.
43. Haniu, H.; Matsuda, Y.; Takeuchi, K.; Kim, Y. A.; Hayashi, T.; Endo, M. Proteomics-Based Safety Evaluation of Multi-Walled Carbon Nanotubes. *Toxicol Appl Pharmacol* **2010**, 242, 256-62.
44. Montezano, A. C.; Touyz, R. M. Mechanosensitive Regulation of Cortactin by P47phox: A New Paradigm in Cytoskeletal Remodeling. *Circ Res* **2013**, 112, 1522-5.
45. Shvedova, A. A.; Kisin, E. R.; Murray, A. R.; Kommineni, C.; Castranova, V.; Fadeel, B.; Kagan, V. E. Increased Accumulation of Neutrophils and Decreased Fibrosis in the Lung of

Nadph Oxidase-Deficient C57bl/6 Mice Exposed to Carbon Nanotubes. *Toxicol Appl Pharmacol* **2008**, 231, 235-40.

46. Elgrabli, D.; Abella-Gallart, S.; Robidel, F.; Rogerieux, F.; Boczkowski, J.; Lacroix, G. Induction of Apoptosis and Absence of Inflammation in Rat Lung after Intratracheal Instillation of Multiwalled Carbon Nanotubes. *Toxicology* **2008**, 253, 131-136.

47. Li, J. G.; Li, W.-X.; Xu, J.-Y.; Cai, X.-Q.; Liu, R.-L.; Li, Y.-J.; Zhao, Q.-F.; Li, Q.-N. Comparative Study of Pathological Lesions Induced by Multiwalled Carbon Nanotubes in Lungs of Mice by Intratracheal Instillation and Inhalation. *Environmental Toxicology* **2007**, 22, 415-421.

48. Mitchell, L. A.; Gao, J.; Vander Wal, R.; Gigliotti, A.; Burchiel, S. W.; McDonald, J. D. Pulmonary and Systemic Immune Response to Inhaled Multiwalled Carbon Nanotubes. *Toxicol Sci* **2007**, 100, 203-214.

49. Shvedova, A. A.; Kisin, E. R.; Murray, A. R.; Gorelik, O.; Arepalli, S.; Castranova, V.; Young, S. H.; Gao, F.; Tyurina, Y. Y.; Oury, T. D., *et al.* Vitamin E Deficiency Enhances Pulmonary Inflammatory Response and Oxidative Stress Induced by Single-Walled Carbon Nanotubes in C57bl/6 Mice. *Toxicol Appl Pharmacol* **2007**, 221, 339-48.

50. Baaziz, W.; Begin-Colin, S.; Pichon, B. P.; Florea, I.; Ersen, O.; Zafeiratos, S.; Barbosa, R.; Begin, D.; Pham-Huu, C. High-Density Monodispersed Cobalt Nanoparticles Filled into Multiwalled Carbon Nanotubes. *Chemistry of Materials* **2012**, 24, 1549-1551.

51. Baaziz, W.; Liu, X.; Florea, I.; Begin-Colin, S.; Pichon, B. P.; Ulhaq, C.; Ersen, O.; Soria-Sanchez, M.; Zafeiratos, S.; Janowska, I., *et al.* Carbon Nanotube Channels Selectively Filled with Monodispersed Fe₃-Xo₄ Nanoparticles. *Journal of Materials Chemistry A* **2013**, 1, 13853-13861.

52. Ricolleau, C.; Nelayah, J.; Oikawa, T.; Kohno, Y.; Braid, N.; Wang, G.; Hue, F.; Florea, L.; Pierron Bohnes, V.; Alloyeau, D. Performances of an 80-200 Kv Microscope Employing a Cold-Feg and an Aberration-Corrected Objective Lens. *Microscopy (Oxf)* **2013**, 62, 283-93.

53. Attal, S.; Thiruvengadathan, R.; Regev, O. *Anal. Chem.* **2006**, 78, 8098-104.

Graphical abstract

